THE ASTRONOMICAL JOURNAL, 121:2173–2184, 2001 April

AB DOR IN '94. I. *HUBBLE SPACE TELESCOPE* GODDARD HIGH RESOLUTION SPECTROGAPH OBSERVATIONS OF THE QUIESCENT CHROMOSPHERE OF AN ACTIVE STAR

J. C. BRANDT,[1,2,3] S. R. HEAP,[1,4] F. M. WALTER,[1,5] E. A. BEAVER,[1,6] A. BOGGESS,[1,7] K. G. CARPENTER,[1,4] D. C. EBBETS,[1,8] J. B. HUTCHINGS,[1,9] M. JURA,[1,10] D. S. LECKRONE,[1,4] J. L. LINSKY,[1,11] S. P. MARAN,[1,12] B. D. SAVAGE,[1,13] A. M. SMITH,[1,4] L. M. TRAFTON,[1,14] R. J. WEYMANN,[1,15] D. NORMAN,[5] AND S. REDFIELD[11]

Received 2000 October 19; accepted 2000 December 14

ABSTRACT

We analyze *Hubble Space Telescope*/Goddard High Resolution Spectrograph spectra of AB Doradus, the prototypical, ultrarapidly rotating K dwarf. We observed chromospheric (Mg II) and transition-region (C II, Si IV, C IV, and N V) lines periodically throughout the stellar rotation period and provide a low-dispersion stellar atlas of 78 emission lines. The quiescent line profiles of the chromospheric and transition-region lines show narrow cores superposed on very broad wings. The broad wings of the Mg II *k* and *h* lines and of the transition-region lines can be explained by emission from gas corotating with the star and extending out to near the Keplerian corotation radius (2.8 stellar radii). While this is not a unique solution, it is consistent with previous studies of Hα emission, which are naturally explained by large corotating prominences. We find no evidence for rotational modulation of the emission-line fluxes. The density diagnostics suggest that the transition region is formed at constant pressure, with an electron density of 2–3 $\times$ 10^{12} cm^{-3} at a temperature of 3 $\times$ 10^4 K. The electron pressure is about 100 times larger than that for the quiet Sun. The emission-measure distribution shows a minimum between log $T = 5$ and 5.5. The Mg II line exhibits three interstellar absorption components along the 15 pc line of sight. We identify the lowest velocity component with the G Cloud, but the other components are not identified with any interstellar clouds previously detected from other lines of sight.

Key words: ISM: kinematics and dynamics — stars: activity — stars: chromospheres — stars: individual (AB Doradus)

1. INTRODUCTION

We study magnetically active solar-like stars because the characteristics of such stars may provide insights into the nature of solar-like magnetic activity. While we accept the solar paradigm that stellar activity is a consequence of magnetic fields, it is not at all clear that any simple scaling of solar coronal structures can account for the level of activity seen in the most active stars. Indeed, the very assumption of solar-like structures may bias our interpretation of the observations. Walter & Byrne (1997), and Walter (1999) proposed a nonsolar paradigm for active stars, based in part on observations of AB Doradus. In this picture, a quasi-dipolar global magnetic field may dominate the large-scale activity, while the hotter coronal gas is confined by solar-like magnetic structures to a small scale height. An active stellar atmosphere would then consist of a compact, solar-like chromosphere/transition region/corona and an extended, corotating envelope of large volume. Ayres et al. (1998) posit a similar picture for the magnetospheres of active Hertzsprung gap giants.

Ultraviolet spectra sample the chromosphere and transition region, at temperatures from about 10^4 through 2×10^5 K. While emission in the cooler lines may result, in part, from heating by acoustic fluxes, the transition-region line emission is almost certainly from hot plasma trapped in magnetic loops. Time-resolved spectra obtained over a stellar rotation can yield important constraints on magnetic filling factors, global asymmetries, and atmospheric scale heights. Velocity-resolved line profiles can be inverted to yield spatial resolution on these stars, as well as images of their surfaces. Our goal, through detailed observations of highly active stars, is to test our understanding of stellar coronae and chromospheres, the morphology of the magnetic field, and its relation to the observed activity.

1.1. *AB Doradus*

AB Doradus (HD 36705; K0–2 IV–V), the brightest ($V = 6.7$) of the ultrarapid rotators ($P_{\rm rot} = 0.51479$ days;

[1] GHRS Investigation Definition Team.
[2] Laboratory for Atmospheric and Space Physics, Campus Box 392, University of Colorado, Boulder, CO 80309-0392; jbrandt@as.unm.edu.
[3] Current address: Department of Physics and Astronomy, Institute for Astrophysics, University of New Mexico, 800 Yale Boulevard, NE, Albuquerque, NM 87131.
[4] Laboratory for Astronomy and Solar Physics, Goddard Space Flight Center, Code 681, Greenbelt, MD 20771; hrsheap@stars.gsfc.nasa.gov, carpenter@stars.gsfc.nasa.gov, hrsleckrone@hrs.gsfc.nasa.gov, hrssmith@hrs.gsfc.nasa.gov.
[5] Department of Physics and Astronomy, State University of New York at Stony Brook, Stony Brook, NY 11794-3800; fwalter@astro.sunysb.edu, dnorman@sbast3.ess.sunysb.edu.
[6] Center for Astrophysics and Space Sciences, University of California, San Diego, C-0111, La Jolla, CA 92093-0111; ebeaver@ucsd.edu.
[7] 2420 Balsam Drive, Boulder, CO 80304; boggess@lyrae.colorado.edu.
[8] Ball Aerospace and Technologies Corporation, PO Box 1062, AR1, Boulder, CO 80306; debbets@ball.com.
[9] Dominion Astrophysical Observatory, 5071 West Saanich Road, Victoria, V8X 4M6 BC, Canada; john.hutchings@hia.nrc.ca.
[10] Department of Physics and Astronomy, University of California, Los Angeles, Los Angeles, CA 90095-1562; jura@clotho.astro.ucla.edu.
[11] JILA, University of Colorado and National Institute of Standards and Technology, Boulder, CO 80309-0440; jlinsky@jila.colorado.edu.
[12] Space Sciences Directorate, Code 600, Goddard Space Flight Center, Greenbelt MD 20771; hrsmaran@eclaire.gsfc.nasa.gov.
[13] Department of Astronomy, University of Wisconsin, 475 North Charter Street, Madison, WI 53706; bdsavage@facstaff.wisc.edu.
[14] MacDonald Observatory and Astronomy Department, University of Texas, Austin, TX 78712; lmt@astro.as.utexas.edu.
[15] Observatories of the Carnegie Institution of Washington, 813 Santa Barbara Street, Pasadena, CA 91101; rjw@ociw.edu.

TABLE 1

GHRS OBSERVATION LOG

Root	Date (1994 Nov)	UT (Start)	Grating	Time (sec)	Phase[a]	Notes[b]
Z2I60107	14	23:04:20	Ech-B	256	0.930	1
Z2I60109	14	23:12:23	G160M	1228	0.941	2
Z2I6010B	14	23:36:04	Ech-B	256	0.973	1
Z2I6010D	14	23:43:51	G160M	1228	0.983	3
Z2I6010F	15	00:08:38	Ech-B	256	1.017	1
Z2I6010H	...	...	G160M	1228	...	4
Z2I6010M......	15	00:59:02	Ech-B	256	1.085	1
Z2I6010O	15	01:07:05	G160M	1228	1.096	2
Z2I6010Q	15	01:30:46	Ech-B	256	1.128	1
Z2I6010S.......	15	01:38:33	G160M	1228	1.138	3
Z2I6010U	15	02:05:02	Ech-B	256	1.174	1
Z2I6010W......	...	...	G160M	1228	...	4
Z2I60111	15	02:53:50	Ech-B	256	1.240	1
Z2I60113	15	03:01:47	G160M	1228	1.250	2
Z2I60115	15	03:25:34	Ech-B	256	1.282	1
Z2I60117	15	03:33:21	G160M	1228	1.293	3
Z2I60119	15	03:57:16	Ech-B	256	1.325	1
Z2I6011B	15	04:05:17	G160M	1228	1.336	5
Z2I6011G	15	04:48:38	Ech-B	256	1.394	1
Z2I6011I	15	04:56:35	G160M	1228	1.405	2
Z2I6011K	15	05:20:08	Ech-B	256	1.437	1
Z2I6011M......	15	05:28:17	G160M	1228	1.448	3
Z2I6011O	15	05:52:04	Ech-B	256	1.480	1
Z2I6011Q	15	05:59:58	G160M	1228	1.491	6
Z2I6011V	15	06:43:20	Ech-B	256	1.549	1
Z2I6011X	15	06:51:09	G160M	1228	1.560	2
Z2I6011Z	15	07:14:50	Ech-B	256	1.592	1
Z2I60121	15	07:23:11	G160M	1228	1.603	3
Z2I60123	15	07:46:52	Ech-B	256	1.635	1
Z2I60125	15	07:54:47	G160M	1228	1.646	7
Z2I6012A	15	08:38:08	Ech-B	256	1.704	1
Z2I6012C	15	08:45:51	G160M	1228	1.714	2
Z2I6012E	...	...	Ech-B	256	...	4
Z2I6012G	15	09:17:35	G160M	1228	1.757	3
Z2I6012I	15	09:41:31	Ech-B	256	1.790	1
Z2I6012K	15	09:49:21	G160M	1228	1.800	5
Z2I6012P	15	10:52:38	Ech-B	256	1.885	1
Z2I6012R	...	...	G160M	1228	...	4
Z2I6012T	15	11:22:52	Ech-B	256	1.926	1
Z2I6012V	15	12:45:21	G140L	844	2.038	8
Z2I6012W......	15	13:03:29	G140L	844	2.062	9

[a] Phase at start of observation. Zero phase occurs at HJD 2,444,296.575. The rotation is 10440 plus the phase.

[b] (1) Mg II *h* and *k*; (2) Si IV; (3) C IV; (4) observation failed; (5) Si III], C III]; (6) N V; (7) C II; (8) low-dispersion 1305 Å; (9) low-dispersion 1570 Å.

$v \sin i = 91$ km s^{-1}), is the quintessential active, young, single star. In addition to large flares (see, e.g., Robinson & Collier Cameron 1986), large starspots (Anders, Coates, & Thompson 1992), and large coronal and chromospheric fluxes (Pakull 1981; Vilhu, Gustafsson, & Walter 1991), AB Dor also possesses corotating material at 2–5 stellar radii (Collier Cameron & Robinson 1989), in the form of cool prominences or Hα clouds (Collier Cameron et al. 1990). Its brightness and activity levels make it an ideal target for studying the extremum of stellar magnetic activity. Among the recent studies are those by Rucinski et al. (1995b), Mewe et al. (1996), Kürster et al. (1997), Schmitt, Cutispoto, & Krautter (1998), Vilhu et al. (1998), and Ake et al. (2000).

The parallax (Guirado et al. 1997) places the star at 15 pc, slightly above the zero-age main sequence (Collier Cameron & Foing 1997), with a probable age close to that of the Pleiades. AB Dor is a member of a multiple-star system. The dMe4 star Rossiter 137B (AB Dor B) is a common proper motion companion at an angular distance of 10″ (Innis et al. 1985; Innis, Thompson, & Coates 1986; Vilhu et al. 1989). Guirado et al. (1997) detected a low-mass astrometric companion, AB Dor C, with an inferred separation of a few tenths of an arcsecond. R 137B is outside the Goddard High Resolution Spectrograph's (GHRS) aperture; AB Dor C falls within the aperture but is unlikely to make any significant contribution to the observed flux.

1.2. *1994 November Campaign*

We observed AB Dor with the GHRS (Brandt et al. 1994; Heap et al. 1995; Robinson et al. 1998) aboard the *Hubble Space Telescope* (*HST*) as part of a multiwavelength campaign in 1994 November (Walter et al. 1995). Our goal was to obtain simultaneous spectroscopic and photometric observations at X-ray, UV, optical, and radio wavelengths over at least one stellar rotation period in order to correlate the coronal, chromospheric, and optical behaviors and come up with a three-dimensional picture of the atmosphere of a very active star.

The optical spectroscopy and photometry and the Doppler images have been reported by Collier Cameron et al. (1999). AB Dor behaved normally (for AB Dor). There was a prominent photometric wave, indicating a highly asymmetric starspot distribution. We observed no large flares (i.e., flares with durations in excess of about an hour). Collier Cameron et al. (1999) report a number of strong absorption events due to cool material (extended prominences) corotating at high altitude. The Doppler image (Collier Cameron et al. 1999) shows a dark feature at high latitudes, with some low-latitude spottedness. Vilhu et al. (1998) report a continuous GHRS observation of the C IV line, immediately preceding our observations.

We will report on the variability of the chromosphere and corona in a subsequent paper (Walter et al. 2001). Here we present an analysis of the quiescent chromosphere of AB Dor as viewed over one stellar rotation period by the GHRS instrument on *HST*.

2. OBSERVING PROGRAM AND DATA REDUCTIONS

We observed AB Dor (program 5181) with the *HST*/GHRS on 1994 November 14–15 while the target was in the continuous viewing zone. The observations began near the end of stellar rotation cycle 10440.[16] Our strategy was to maximize spectral and temporal coverage by rapidly changing gratings to obtain a sequence of exposures during the 12.3 hr rotation period of AB Dor. For 12 hr we alternated between 256 s integrations of the Mg II lines using the echelle B ($R \equiv \lambda/\delta\lambda \sim 100{,}000$) and 1228 s integrations of transition-region lines using the G160M first-order grating ($R \sim 20{,}000$). This strategy was driven by the one-dimensional format of the GHRS detectors; at $R = 20{,}000$ we observe only about 35 Å at a time.

The main observation was split into six sequences. Each sequence began with a peak-up in the large aperture, to ensure that the target remained well centered. Each sequence then consisted of three observations of the Mg II line, alternating with observations of the Si IV $\lambda\lambda$1393, 1402 doublet, the C IV $\lambda\lambda$1548, 1551 doublet, and either the N V $\lambda\lambda$1238, 1242 doublet, the C II $\lambda\lambda$1334, 1335 doublet, or the density-sensitive Si III], C III] $\lambda\lambda$1892, 1908 intersystem lines. We concluded these six sequences with a final Si IV exposure sandwiched between two Mg II observations. All these observations used the D2 detector. At the end of these sequences, we changed to the D1 detector and observed the full short-wavelength spectrum (1150–1750 Å) at low dispersion in two G140L exposures. The details of the exposures are given in Table 1. Four observations were lost when the carousel failed to lock.

Each science observation was preceded by a spectral calibration lamp exposure that established the accurate wavelength scale. Occasional SPYBAL observations of the wavelength-calibration lamps were also interspersed by the scheduling software. The target was observed through the Large Science Aperture (LSA) using substep pattern 5. We calibrated the raw data using the GHRS team software procedure CALHRS (Blackwell et al. 1993). Each Mg II observation is a single spectrum, but each transition-region spectrum consists of four independent spectra, providing about 5 minute temporal resolution. The analysis of the line profiles (excluding the Mg II interstellar medium [ISM] analysis in § 9) was carried out using the ICUR software package.[17] All the measurements (fluxes, centroids, Gaussian fits) use standard techniques.

Mewe et al. (1996) fit the *Extreme Ultraviolet Explorer* (*EUVE*) and *ASCA* spectra, and found a best-fit absorption column of $2.4 \pm 0.5 \times 10^{-18}$ cm^{-2}. Since the reddening correction is less than 1%, we do not apply any reddening corrections.

3. LOW-DISPERSION SPECTRAL ATLAS

The summed low-dispersion spectrum is shown in Figure 1. Two spectra centered at 1305 and 1571 Å cover almost all the useful wavelength range of the G140L grating (1162–1714 Å) with 20 Å of overlap in the middle. The resolution of this spectrum, $R \sim 2000$, is adequate to resolve most astrophysically important blends, including (marginally) the C II $\lambda\lambda$1334, 1335 doublet. We obtained this spectrum primarily for the purpose of constructing the line atlas (Table 2) and for determining the emission-measure distribution (§ 8) of the chromosphere of this very active star.

The spectrum shows a wealth of detail, including weak lines of neutral and low-ionization species, the strong transition-region lines, and the Fe XXI coronal line. We have identified the emission lines using the solar line lists of

[16] Using the ephemeris HJD = 2,444,296.575 + 0.51479*E*.

[17] See http://sbast3.ess.sunysb.edu/fwalter/ICUR/icur.html.

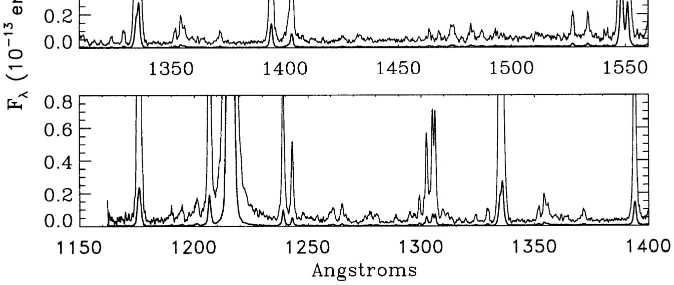

FIG. 1.—Summed low-dispersion G140L spectrum of AB Dor between 1162 and 1714 Å, smoothed with a Fourier filter. The data are binned into 0.14 Å bins. The flux scale refers to the thin line; the heavy line is scaled down by a factor of 10 to show the full dynamic range in the spectrum. Between 1428 and 1448 Å, where the spectra overlap, the effective exposure time is 1688 s; elsewhere the exposure time is 844 s. Much of the Lyα emission is geocoronal. Geocoronal O I λ 1304 is seen as a low broad pedestal under the narrow stellar lines.

TABLE 2

LOW-DISPERSION LINE ATLAS

λ	Flux (10^{-14} ergs cm^{-2} s^{-1})	Line Identification
1175.86 ...	44.0 ± 0.4	C III λ1175.711
1189.86 ...	1.43 ± 0.28	S III λ1190.17, Si II λ1190.42
1194.41 ...	1.68 ± 0.29	Si II λ1193.29, S III λλ1194.06, 1194.46
1197.56 ...	0.40 ± 0.18	Si II λ1197.39
1201.13 ...	2.77 ± 1.14	N I λλ1200.22, 1200.71, S III λλ1200.97, 1201.73
1206.68 ...	24.9 ± 0.7	Si III λ1206.51
1215.91 ...	...	H I (⊕)
1238.99 ...	13.7 ± 0.28	N V λ1238.82
1243.05 ...	6.62 ± 0.25	N V λ1242.80
1247.81 ...	0.28 ± 0.16	C III λ1247.38
1253.96 ...	0.31 ± 0.10	Si II λ1253.80
1259.57 ...	0.96 ± 0.09	Si II λ1259.53
1261.08 ...	1.01 ± 0.08	C I λ1261.3
1264.81 ...	1.46 ± 0.09	Si II λ1264.74
1266.50 ...	0.74 ± 0.09	C I λ1266.42
1275.04 ...	0.52 ± 0.07	...
1277.33 ...	1.19 ± 0.08	C I λ1277.5
1280.14 ...	0.98 ± 0.09	C I λ1280.5
1288.77 ...	0.64 ± 0.15	C I λ1288.42
1294.87 ...	0.70 ± 0.20	Si III λ1294.54
1296.77 ...	0.46 ± 0.28	Si III λ1296.72
1299.09 ...	1.31 ± 0.30	Si III λ1298.89
1301.16 ...	0.64 ± 0.07	Si III λ1301.15
1302.33 ...	5.27 ± 0.10	O I λ1302.16
1304.97 ...	5.27 ± 0.15	O I λ1304.86
1306.12 ...	7.06 ± 0.15	O I λ1306.03
1309.59 ...	0.90 ± 0.08	Si II λ1309.28
1311.53 ...	0.70 ± 0.09	C I λ1311.36
1313.35 ...	0.30 ± 0.08	...
1316.67 ...	0.19 ± 0.06	S I λ1316.54
1319.46 ...	0.13 ± 0.06	N I λ1319.00
1323.99 ...	0.57 ± 0.16	S I λ1323.52
1329.28 ...	1.17 ± 0.07	C I λ1329.1
1334.74 ...	22.8 ± 0.2	C II λ1334.53
1335.83 ...	35.2 ± 0.2	C II λ1335.71
1351.76 ...	1.34 ± 0.08	Cl I λ1351.66
1354.16 ...	1.90 ± 0.08	Fe XXI λ1354.08
1355.71 ...	1.83 ± 0.10	O I λ1355.60
1358.91 ...	0.92 ± 0.10	C I λ1357.13, O I λ1358.51
1361.63 ...	0.27 ± 0.05	...
1363.27 ...	0.29 ± 0.06	...
1364.44 ...	0.37 ± 0.06	C I λ1364.16
1370.27 ...	0.14 ± 0.05	N III λ1369.99
1371.53 ...	1.06 ± 0.12	O V λ1371.292
1393.89 ...	21.3 ± 0.05	Si IV λ1393.76
1399.72 ...	0.65 ± 0.10	O IV] λ1399.77
1401.34 ...	1.24 ± 0.15	O IV] λ1401.16
1402.90 ...	12.0 ± 0.13	Si IV λ1402.77
1407.68 ...	0.24 ± 0.10	O IV] λ1407.39
1412.59 ...	0.34 ± 0.10	Fe II λ1412.83
1416.71 ...	0.25 ± 0.08	S IV] λ1416.93
1424.04[a] ...	0.14 ± 0.07	S IV] λ1423.9
1425.41 ...	0.73 ± 0.11	S I λ1425.03
1432.43 ...	1.07 ± 0.10	C I λ1432.11
1459.14 ...	0.11 ± 0.10	C I λ1459.03
1463.72 ...	1.02 ± 0.13	C I λ1463.33, Fe X λ1463.50
1468.00 ...	0.79 ± 0.16	Fe IX λ1467.06, C I λ1467.4
1473.12 ...	0.88 ± 0.12	S I λ1472.97
1474.36 ...	1.22 ± 0.13	S I λ1474.00
1481.93 ...	1.12 ± 0.13	S I λ1481.67
1483.27 ...	0.33 ± 0.08	S I λ1483.23
1486.89 ...	0.90 ± 0.13	N IV λ1486.50, S I λ1487.15
1492.98...	0.85 ± 0.13	...
1526.89...	2.14 ± 0.13	Si II λ1526.71
1533.66...	2.71 ± 0.61	Si II λ1533.43
1540.84...	0.22 ± 0.10	Fe II λ1541.03
1542.26...	0.27 ± 0.09	C I λ1542.18
1548.40...	80.9 ± 0.7	C IV λ1548.20
1550.94...	42.7 ± 0.6	C IV λ1550.77
1561.09...	9.31 ± 0.24	C I λ1561.00
1640.52...	84.7 ± 0.89	He II λ1640.48
1649.98...	0.54 ± 0.19	Fe II λλ1649.42, 1649.57
1657.33...	38.0 ± 0.71	C I λλ1556.28, 1556.97, 1557.38, 1558.01
1666.70...	1.52 ± 0.19	O III] λ1666.15
1670.86...	5.87 ± 0.25	Fe II λ1670.74
1686.79...	0.42 ± 0.19	Fe II λ1686.46
1697.03...	2.40 ± 0.34	Fe II λ1696.79
1713.18...	1.64 ± 0.13	Fe II λ1713.0

[a] Wavelength fixed; blended with S I λ1425.03.

Burton & Ridgeley (1970) and Feldman et al. (1997). Other possible identifications are found in the CHIANTI (Dere et al. 1997) database. The brightest stellar emission line is He II 1640 Å (the H I Lyα emission is geocoronal). Identifications for some of the weaker lines and blends are uncertain and will require higher dispersion spectra for definitive identification.

There are 63 lines in Table 2 with secure identifications. The mean difference between the observed and tabulated (rest) wavelengths is 0.15 ± 0.02 Å, corresponding to a radial velocity of 33 ± 5 km s^{-1}, which is in good agreement with the previously measured photospheric value of 30 km s^{-1}. Much of the scatter lies, as expected, in the weaker lines. The mean radial velocity of the 34 strongest lines (fluxes greater than 1.0×10^{-14} ergs cm^{-2} s^{-1}) is also 33 ± 5 km s^{-1}. This agreement with the photospheric radial velocity verifies that the wavelength scale is accurate and that the line identifications are most likely correct.

4. 1900 Å REGION

Figure 2 shows the mean spectrum in the 1900 Å region. The two G160M observations were obtained at rotational phases 0.336 and 0.800, and sampled opposite hemispheres of the star. The 1900 Å continuum is 46% brighter at phase 0.8. The contemporaneous *U*- and *V*-band photometry (Rucinski, Garrison, & Duffee 1995a; Collier Cameron et al. 1999) shows that the star was faintest at about rotation phase 0.5, and that in the *U* band AB Dor is about 15% brighter at phase 0.8 than at phase 0.34. There is no significant change in the emission-line fluxes between the two observations.

In addition to the expected Si III] λ1892 and C III] λ1908 intersystem lines, we see four narrow lines of S I and a line of Si I (Table 3, Fig. 2). The possible feature at 1907.3 Å (1907.1 Å rest wavelength) is unidentified.

The C III] λ1908 line is much broader than the other lines (see § 7.4). The line widths listed in Table 3 are measured by fitting Gaussians to the lines. A line broadened by the stellar rotation would have a FWHM of approximately 0.8 Å in this spectral region (assuming a 40% overestimate of $v \sin i$ from the Gaussian fit; see discussion in § 5).

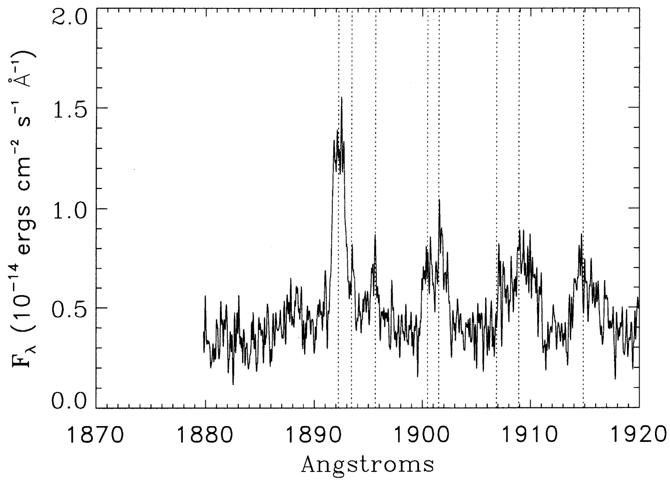

FIG. 2.—Mean G160M spectrum of the 1900 Å region. The two observations have been averaged, and a Fourier filter has been applied. In addition to the Si III] λ1892.03 and C III] λ1908.734 lines, we see emission of S I λλ1893.252, 1895.459, 1900.27, 1914.68, and Si I λ1901.338. There appears to be a narrow emission line at 1907.34 Å. The C III] λ1908.734 line is broader than the other lines, perhaps because it arises in low-density regions well above the photosphere but corotating with the star. The dotted vertical lines mark the rest wavelengths of these lines at the stellar radial velocity.

5. TRANSITION-REGION QUIESCENT LINE PROFILES

We monitored the transition-region doublets of C II, Si IV, C IV, and N V. The Si IV and C IV lines were each observed six times and exhibited variability. Each observation consisted of four ∼5 minute integrations, which permitted us to examine the data for line profile variations or flaring on timescales of 5–20 minutes. We examined the individual integrations for evidence of flaring (rapid flux variations over the four integrations, varying line profiles, or fluxes significantly in excess of the median). We generated quiescent line profiles by summing those spectra that had fluxes near the median, symmetric line profiles, and no evidence for flaring. In Figure 3, we compare the four quiescent line profiles. Here we discuss only the quiescent line profiles; we will discuss the flaring spectra elsewhere.

We initially fitted the emission lines as Gaussians or sums of Gaussians because this approach is commonly used and the resulting fits are generally quite acceptable. Vilhu et al. (1998) found that the C IV emission lines could be fitted as a sum of narrow and broad Gaussian components (as found, in general, by Wood, Linsky, & Ayres 1997). The narrow components are significantly broader than the expected rotational broadening, and Vilhu et al. interpreted this non-

TABLE 3

LINES IN 1900 Å SPECTRAL REGION

λ[a]	Flux (10^{-14} erg cm^{-2}s^{-1})	FWHM (Å)	Line Identification
1892.30 ± 0.01......	1.51 ± 0.01	1.28 ± 0.05	Si III] λ1892.030
1893.58 ± 0.02......	0.09 ± 0.02	0.26 ± 0.07	S I λ1893.252?
1895.39 ± 0.02......	0.52 ± 0.03	0.63 ± 0.09	S I λ1895.459
1900.48 ± 0.02......	0.34 ± 0.01	0.81 ± 0.13	S I λ1900.270
1901.74 ± 0.01......	0.54 ± 0.01	0.94 ± 0.10	Si I λ1901.338
1907.34 ± 0.04......	0.25 ± 0.02	0.88 ± 0.16	...
1909.38 ± 0.04......	1.1 ± 0.1	2.09 ± 0.15	C III] λ 1908.734[b]
1915.05 ± 0.04......	0.75 ± 0.03	0.87 ± 0.24	S I λ1914.680

[a] Observed wavelength. The rest wavelengths are 0.19 Å smaller.
[b] Broad line. See discussion in § 7.4.

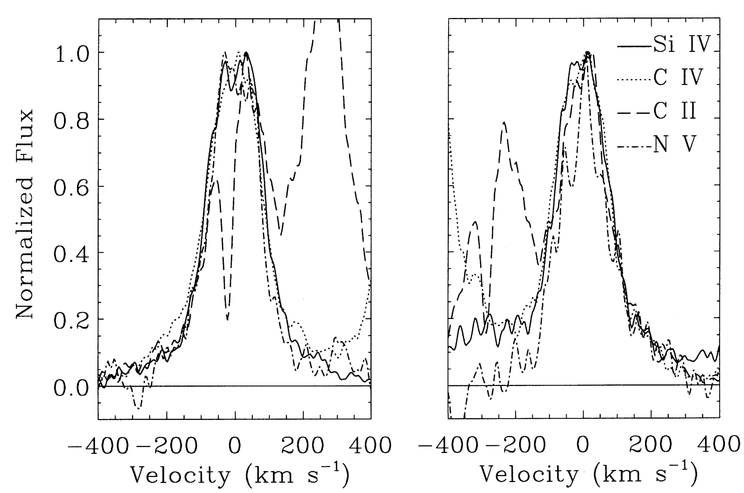

FIG. 3.—Comparison of the four transition-region doublets in velocity space. The left panel shows the blueward line; the right panel shows the redward line. The normalized profiles are similar, with the following exceptions: the C II λ1334 emission line includes a strong interstellar absorption feature; the blue wing of the Si IV λ1402 line (*right panel*) is elevated because of O IV emission; and the N V λ1242 line is noisy. The other component of the C II doublet is visible in each panel, and the wings of the C IV lines overlap.

thermal broadening in terms of solar-like nonthermal broadening mechanisms (see, e.g., Dere & Mason 1993), perhaps related to microflares. Unlike the case of the Sun, we do not know much about the spatial distribution of the emitting gas. It probably is not confined to a thin region, given the evidence for extended prominences, in which case the atmosphere is extended and interpretation of line profiles is not straightforward.

We simulated line profiles from photospheres (with limb-darkening parameters $-1.0 < \epsilon < 1.0$) and optically thin, extended, corotating atmospheres, convolved them with the expected thermal broadening and a Gaussian instrumental response, and fitted the lines as Gaussians. In the case of $\epsilon = 0.6$, we recover the well-known rotational profile (see, e.g., Gray 1992); $\epsilon = 0.0$ is a uniform disk, and $\epsilon < 0$ yields limb-brightened profiles. Transition-region lines are more likely optically thin emissions from an extended atmosphere. We also examined cases in which the emission was confined to low latitudes. Limb-brightened atmospheres tend to produce flat-peaked line profiles (for modest extents of $\lesssim 10\%$ of the stellar radius), whereas limb-brightened atmospheres with emission confined to low latitudes produce emission cusps for sufficiently large $v \sin i$.

Although the intrinsic line profiles are not Gaussian, significant noise and low resolving power allow Gaussian fits to be acceptable in many cases. The widths of the Gaussian fits always exceed $v \sin i$. We find that for photospheric line profiles, the Gaussian fits overestimate $v \sin i$ by up to 40%, depending on the value of ϵ and the intrinsic $v \sin i$. Gaussian fits to limb-brightened profiles (containing a few thousand counts) overestimate the $v \sin i$ by 40%–80%. Dere & Mason (1993) showed that optical thickness will also tend to broaden the line profiles; in slightly thick but effectively thin lines, photons from the line core will be scattered into the wings. We caution the reader that the interpretation of emission-line profiles is highly model dependent. Consequently, we do not interpret the width of the narrow emission component of the transition-region lines.

In Figure 4, we show the subordinate $(3p\ ^2P_{1/2}$–$3d\ ^2D_{3/2})$ Mg II line at 2791.6 Å, which is almost certainly optically thin. The profile is flat topped, and at resolution $R \sim 10^5$, the shape of the line profile is clearly not Gaussian. The rotation profile for a limb-darkened photosphere is much more sharply peaked. Figure 4 demonstrates that this line can be produced by a limb-brightened, optically thin atmosphere with a height of a few percent of the stellar radius. This fit is not unique: within the uncertainties, one could also fairly well reproduce the profile with, for example, a rotating photospheric profile ($\epsilon = 0.6$) with no emission above about 30° latitude, or a uniform disk profile ($\epsilon = 0.0$) with emission confined below about 60° latitude.

The strong resonance lines of the transition region clearly cannot be fitted with a single component. Instead, we fit the lines as sums of narrow and broad Gaussians. We find that we get better fits with three components: one broad component and two similar narrow Gaussians displaced from line center by about $\pm 0.5 v \sin i$. This model gives better fits because the peaks of the Si IV and C IV are flatter than a Gaussian profile. Physically, this is because in an extended limb-brightened atmosphere, the centroid of the emission is displaced to higher velocities, where the path length through the atmosphere is longer. We also have had success in fitting the line wings with emission from an optically thin, extended, rigidly rotating atmosphere (see § 5.5).

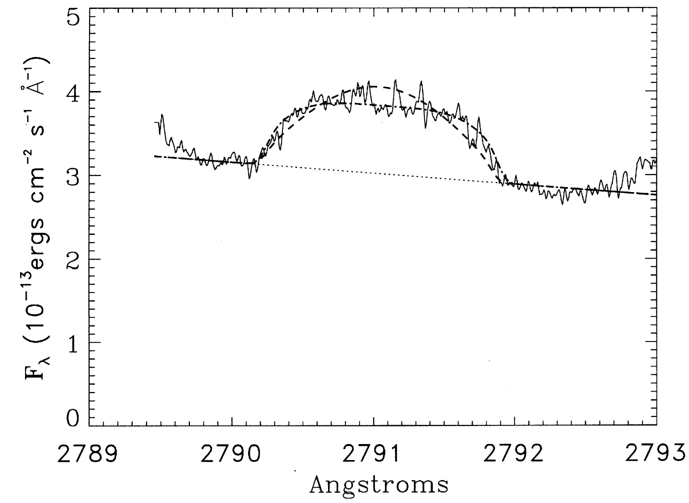

FIG. 4.—Subordinate 2791 Å line of Mg II. The data are the mean of 19 echelle observations. This line is almost certainly optically thin and therefore represents the convolution of the surface distribution of Mg II with the rotational and thermal broadening. We show two fits to this line. The narrower profile (*dashed line*) is the rotational profile for a limb-darkened surface ($\epsilon = 0.6$); the broader profile (*dot-dashed line*), which better matches the data, is a limb-brightened atmosphere with a height of 2% of the stellar radius. Both profiles are rotationally broadened, with $v \sin i = 90$ km s^{-1}, and have 5 km s^{-1} of thermal broadening. There is no evidence for nonthermal broadening at this level of the atmosphere. The dotted line is the extrapolated continuum.

5.1. C IV

We identified 17 of the 24 C IV integrations as likely to represent the nonflaring, quiescent transition region. The C IV flux (the sum of the fluxes in the $\lambda\lambda 1548$, 1551 lines) during quiescence is less than 1.5×10^{-12} ergs cm^{-2} s^{-1}. Vilhu et al. (1998) noted that the nonflaring flux level just prior to our observation ranged between 1.0 and 1.5×10^{-12} ergs cm^{-2} s^{-1}, and the average C IV flux during our entire observation was 1.2×10^{-12} ergs cm^{-2} s^{-1}. The $\lambda\lambda 1549/1551$ line ratio of 1.78 ± 0.03 is close to but less than the optically thin limit.

The summed quiescent line profile (Fig. 5) should represent the phase-averaged transition region. Although we can fit the line with a sum of two Gaussians with fit parameters similar to those of Vilhu et al. (1998), we find that the data are better fitted with three components.

We do not plot the two- or three-component Gaussian fits to this or any line in Figures 5–7. Rather, the fits to the high-velocity wings shown in Figure 5 are for optically thin, constant-density atmospheres, extending out 2.5 stellar radii. Forty percent of the total flux is in the extended component.

5.2. Si IV

The mean Si IV $\lambda 1393$ line flux is 2.2×10^{-13} ergs cm^{-2} s^{-1}. From a visual examination of the line profiles and line fluxes, we identified 20 quiescent spectra and summed these (Fig. 6). The $\lambda 1393/\lambda 1402$ line ratio of 1.78 ± 0.02 is identical to that in the C IV lines. Although close to the optically thin limit, both line ratios are significantly less than 2. This probably indicates that at least some of the emission is from optically thick regions.

Because the lines are well separated and because the blue wing of the 1402 Å line is blended with O IV] $\lambda 1401.34$, we

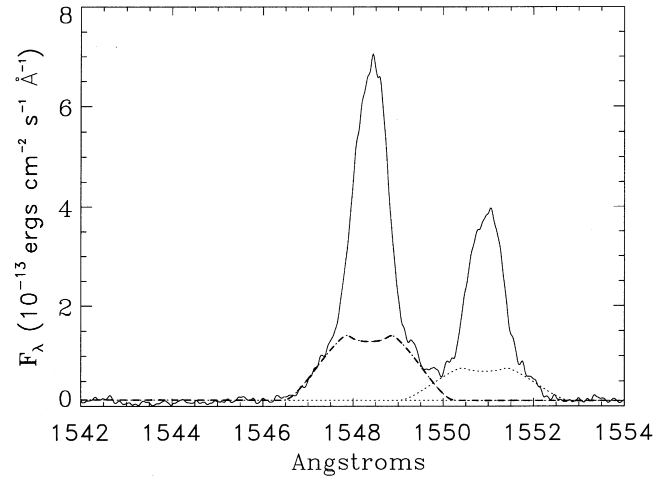

FIG. 5.—Mean quiescent C IV line profiles. The data have been smoothed with a Fourier filter. The dashed and dotted lines represent a model for emission from an optically thin, constant-density atmosphere extending out to 3 stellar radii. The model is centered on the rest wavelength of the line and is scaled to the blue wing. The 1551 Å line is not fit but is assumed to be half the intensity of the 1548 Å line.

fitted only the 1393 Å line. As with the C IV lines, the Si IV line profile is better fitted with a broad component, centered on the rest velocity of the star plus two narrow emission components, than it is with a two-Gaussian model. If we fit the high-velocity wings as emission from extended gas (see Fig. 6), we find that the emission extends out to 3 stellar radii, which is comparable to what we found for C IV. About 25% of the Si IV emission is in the extended component.

5.3. N V

We obtained a single G160M observation of the N V doublet at phase 0.5. The line fluxes are 95% of those seen in the low-dispersion spectrum. The line ratio of 2.10 ± 0.04 is consistent with the line's being optically thin. There is no evidence for the broad component seen in the Si IV and C IV lines, perhaps because of the low signal-to-noise ratio in this integration. However, there is a small flux excess on the red side of the 1242 Å line. This is not seen on the blue side of the line, nor is it obvious in the 1238 Å line. The cause could be a downflow, or perhaps a small flare on the receding limb of the star.

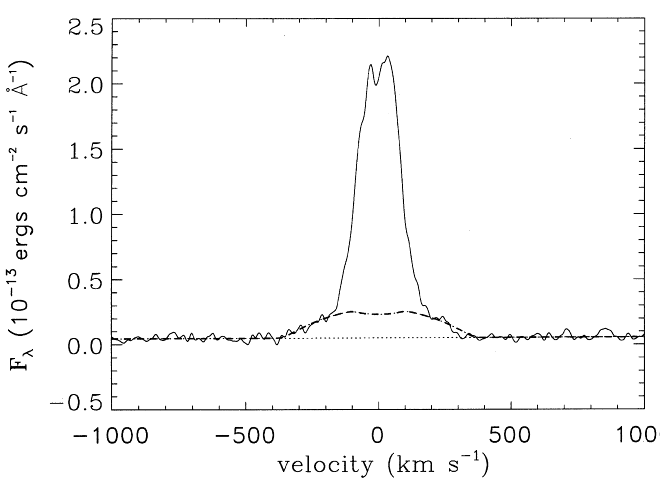

FIG. 6.—Same as Fig. 5, but for Si IV λ1393. The double-peaked line profile is not representative of any individual line, but is the consequence of summing 20 variable line profiles.

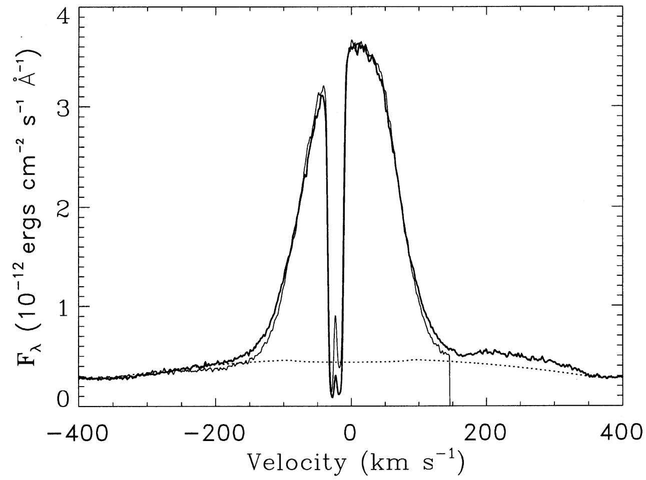

FIG. 7.—Mean Mg II line profiles. The heavy line is the k line; the h line is overplotted as the thin line (the data are cut off at +145 km s^{-1} by the edge of the detector). The h line flux has been multiplied by a factor of 1.23 to match the line cores. The k line is brighter in the wings. The blue wing extends out to about −320 km s^{-1}. The hump on the red wing of the k line (between +170 and +350 km s^{-1}) is the sum of the λ 2797.922 ($3p\ ^2P_{3/2}$–$3d\ ^2D_{3/2}$) and λ 2797.989 ($3p\ ^2P_{3/2}$–$3d\ ^2D_{5/2}$) subordinate lines of Mg II. The dotted line shows the expected emission-line profile for an optically thin uniform density extended atmosphere with a height of 3 stellar radii.

5.4. C II

We obtained a single G160M observation of the C II doublet at phase 0.65. The emission lines are severely blended, and we were unable to fit the various components uniquely. High-velocity wings are evident. There is a strong interstellar absorption feature in the 1334.5 Å line, with a radial velocity of 9 ± 3 km s^{-1}. Given the resolution of the GHRS in this mode, it is not possible to identify the absorption with any particular component of the ISM (see § 9). Corresponding (although much weaker) absorption is seen near the top of the 1335.7 Å line.

This spectrum also shows the S I λ1323.52, C I λ1329.1, and Cl I λ1351.66 lines with fluxes similar to those in Table 2.

5.5. *Discussion of the Transition-Region Lines*

The transition-region lines of active stars are generally modeled as the sum of broad and narrow Gaussians. The width of the narrow component is generally significantly broader than the stellar $v \sin i$, and this is interpreted as the convolution of the stellar rotational profile with some other broadening mechanism. Wood et al. (1997) showed that among dwarf stars, the excess broadening appears to decrease with increasing surface gravity ($\xi_{\rm NC} \propto g^{-0.68}$). The broad component is often interpreted as evidence for high-velocity gas associated with microflaring.

We have difficulty interpreting the line profiles of AB Dor in this manner. After deconvolving the 90 km s^{-1} rotational velocity from the narrow central emission component, we find that the velocity of the excess broadening mechanism is about 120 km s^{-1}, which places AB Dor well above the trend found by Wood et al. (1997) for less active stars. In addition, while microflaring may indeed exist and contribute to the width of the broad component, the evidence for spatially extended gas leads us to propose a fundamentally different mechanism for the broad-line component.

We propose that the high-velocity wings are due to spatially extended gas corotating with the star and not to some unknown broadening mechanism. The existence of extended prominences seen in the light of Hα is well established; it is likely that this same gas accounts for the extended wings of the Mg II *k* and *h* lines. The wings of the transition-region lines have very similar shapes, suggesting that these lines also have a similar origin. Corroborating evidence for extended hot gas exists: Walter et al. (1995, 2001) show that C IV undergoes absorption events associated with Hα prominences.

We model the extended gas as a simple, optically thin volume corotating with the star and assume that the density is uniform between some inner and outer radii. The emission from each point is broadened by a thermal velocity appropriate to the ion in question. The computed profiles do not depend sensitively on the value of the assumed inner radius, since the emission from gas close to the star is hidden by the central emission component, but the outer radius does determine the width of the broad-line component. We vary only the outer radius to match the observations. We can also vary the extent of the gas in latitude, but we are not very sensitive to this because gas at high latitudes has smaller velocities and is buried under the central emission.

The inferred radial extent of the extended gas is close to the Keplerian corotation radius of 2.8 stellar radii. We favor a model in which the gas is trapped by large-scale, quasi-dipolar magnetic fields (Walter 1999). Such gas will be most stable near the corotation radius (e.g., the "slingshot prominences" of Collier Cameron & Robinson 1989).

Assuming that the gas is optically thin and in rigid rotation, we can use the high-velocity wings to estimate the mean electron density in the extended gas. The mean electron density n_e is given by $0.8(L/PV)^{1/2}$, where L is the velocity-resolved luminosity of the line, P is the power in the line, V is the velocity-resolved volume element, and the 0.8 factor accounts for the fact that hydrogen is largely ionized. The mean density is about 5×10^7 cm^{-3} at the temperature of the transition-region lines for a filling factor of 1; the presence of discrete prominences suggests that the filling factor of this extended region is very low, and the density in the prominences must be commensurately larger.

We see no evidence for any rotational modulation of the fluxes in the Mg II, C IV, or Si IV lines. The photosphere is faintest at rotation phase 0.5 (Collier Cameron et al. 1999). Following the solar analogy, the dark regions (starspots) are likely regions of larger photospheric magnetic flux, and the bright chromosphere and transition region should be located above the starspots. If the chromosphere and transition region are spatially extended, as is likely the case here, then any modulation would be diluted. Our data let us place a limit of 5% on the amplitude of the rotational modulation in the chromospheric and transition-region lines.

6. THE Mg II LINES

6.1. *Chromospheric* Mg II *Emission*

We observed the chromospheric Mg II *k* and *h* lines 19 times, approximately every 35–50 minutes, with a resolving power of about 10^5. The mean profile of the two lines is presented in Figure 7. The *k* and *h* resonance lines are well exposed, and the Mg II subordinate lines are detected as well. Both the *k* and *h* lines exhibit extended blue wings, to velocities of about -320 km s^{-1}, with respect to the star. The red wings cannot be measured because the *k* line is blended with the subordinate lines, and the red wing of the *h* line falls off the edge of the detector. The brightness ratio near line center is 1.23, confirming that the line cores are optically thick, and the *k* line has brighter line wings, as expected for the higher opacity line. Over 10% of the flux in the line core is lost to the narrow interstellar absorption lines (see § 9).

Since Mg II is formed in the chromosphere, at about the same temperature as Hα, one might expect to see absorption events in Mg II similar to those seen in Hα (Collier Cameron et al. 1990, 1999), and indeed we do see such absorption events. These will be discussed elsewhere (Walter et al. 2001). The same prominences seen in absorption against the stellar disk should be seen in emission off the limb and could account for the broad wings of the *k* and *h* lines. The maximum velocity is consistent with emission from gas in corotation at heights of up to 3.5 stellar radii. In Figure 7, we overplot the expected emission-line profile, scaled to the data, for a corotating atmosphere extending to a height of 3 stellar radii. This is neither a fit to the data nor a unique description of the data, but it demonstrates that the extended wings could arise from an extended atmosphere without assuming nonthermal broadening mechanisms. This extended emission accounts for 20% of the total Mg II *k* and *h* emission, after correcting for the interstellar absorption. The mean density in the extended atmosphere at chromospheric temperatures is about 3×10^8 cm^{-3} (for a filling factor of 1). This is about a factor of 6 higher than the density inferred from the transition-region lines and is consistent with a constant-pressure atmosphere within the uncertainties.

7. DENSITY DIAGNOSTICS

The mean density at a given temperature provides clues to the gross morphology of the stellar atmosphere, since the emission measure ($\int n_e n_{\rm H}\, dV$) depends on both the density and the volume. Even at very low spatial resolution, the observed density can help us discriminate between compact, high-density emitting regions and large extended structures. There are a number of density diagnostics in this region of the spectrum (see, e.g., Doschek et al. 1978). We use the line strengths in Tables 2, 3, and 4 to compute the density-sensitive line ratios, and we use the CHIANTI software package to convert the line ratios to densities.

7.1. *Densities Involving the* Si III *Lines*

We used 3 Si III lines and the sum of the λλ1294–1301 lines to form four line ratios. These consistently yield den-

TABLE 4

WEAK LINES IN THE G160M 1400 Å SPECTRUM

λ[a]	Flux (10^{-14} erg cm^{-2}s^{-1})	Line Identification
1400.07 ± 0.04......	0.5 ± 0.1	O IV] λ1399.77
1401.58 ± 0.03......	1.2 ± 0.3	O IV] λ1401.16
1407.70 ± 0.02......	0.26 ± 0.04	O IV] λ1407.39

[a] Observed wavelength. The rest wavelengths are 0.14 Å smaller.

sities between 2 and 3×10^{12} cm^{-3} at a temperature of about 3×10^4 K (Table 5).

7.2. *Densities Involving the* C III *Lines*

Cook & Nicolas (1979) discuss using the C III lines to determine densities. We use the 1175, 1247, and 1908 Å lines in this analysis. The densities are not mutually consistent (Table 5). Cook & Nicolas (1979) note that in the Sun the density ratios involving the 1175 Å line are consistently off, perhaps because the 1175 Å line intensity is reduced by optical depth effects. An increase of about a factor of 2 in the 1175 Å line flux would bring the λ1175/λ1908 density into agreement with the λ1247/λ1908 density at about 10^{11} cm^{-3}. The λ1175/λ1247 density would then become about 5×10^{11} cm^{-3}.

Using the λ1175/λ977 line ratio, Schmitt et al. (1998) and Ake et al. (2000) both infer densities at the high-density limit, greater than 10^{11} cm^{-3}, which is consistent with our estimates.

The densities inferred from the C III lines (formed at 6×10^4 K) are smaller than those inferred from Si III (formed at about 3×10^4 K): in a constant-pressure atmosphere, they should have about half the density indicated by the Si III lines. This would be consistent with a model in which the bulk of the transition-region emission arises in constant-pressure loops.

Cook & Nicolas (1979) also estimate densities from ratios of Si III] λ1892 and Si IV λ1402 to C III] λ1908. These densities are valid so long as the relative abundances are solar. The λ1892/λ1908 ratio has traditionally been used as a density diagnostic in *IUE* spectra (Doschek et al. 1978). We find this ratio to be about 1.3, which suggests a density near 3×10^{10} cm^{-3}, but the λ1402/λ1908 ratio implies a density nearer to 3×10^{11} cm^{-3}, using Cook & Nicolas' model atmosphere ratios. Note that the Si III] λ1892 and C III] λ1908 line profiles are very different (Fig. 2), with the C III] line being nearly twice as broad, suggesting that they might not be formed cospatially.

7.3. *Densities from the 1400 Å Region*

The 1400 Å region (Fig. 8) includes a number of density-sensitive O IV] (Cook et al. 1995) and S IV] (Dufton et al. 1982) intercombination lines. These lines are much weaker than the nearby Si IV resonance lines. The 1399.8 and 1401.2 Å O IV] lines are clearly visible in the low-dispersion spectrum, blended with the blue wing of Si IV λ1402.8. We estimated their fluxes first by fitting all three lines, forcing the wavelengths and line widths of the O IV] lines to their expected values. Since the two Si IV lines should have identical profiles, we then shifted, scaled, and subtracted the Si IV λ1393.8 from the Si IV λ1402.8 line profile and fitted the residuals. The 1407.4 Å O IV] line is also visible in the low-dispersion spectrum. These fluxes can be found in Table 2.

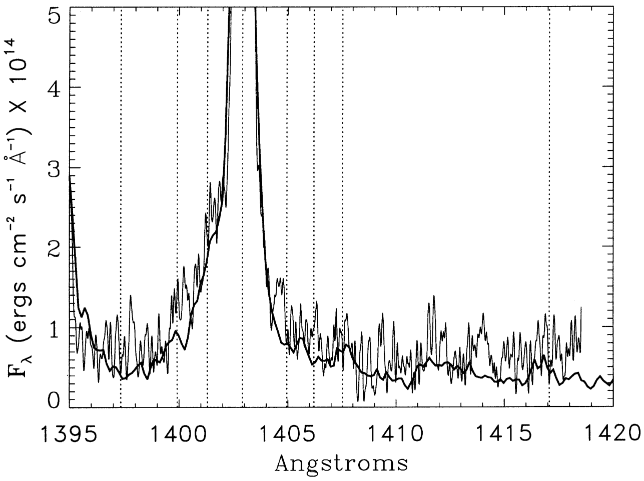

FIG. 8.—Spectra in the 1400 Å region. The thin (noisier) line is the mean of six G160M observations (7368 s integration time); the heavy line is the 844 s G140L spectrum. Both spectra have been smoothed with a Fourier filter. The strong emission line is Si IV λ1402. Vertical dotted lines mark the expected locations of the O IV] and S IV] lines, at the +30 km s^{-1} radial velocity of AB Dor. The clear asymmetry in the blue wing of the Si IV λ1402 line is due to the O IV] λ1399.8 and λ1401.2 lines. There may also be weak detections of O IV] λ1407.4 and S IV] λ1416.9 in the low-dispersion spectrum. The peak at λ1404.6 in the G160M spectrum is at the wrong wavelength to be the λ1404.8 O IV] + S IV] blend. The other O IV] and S IV] lines are not detected in either spectrum.

We also searched for these lines in the summed G160M spectrum (total exposure time is 7368 s). This spectrum is a global average over all rotational phases. Although flaring affects the strong Si IV resonance line profiles and fluxes, we find no evidence of enhanced emission in the weaker lines during flares. As in the low-dispersion image, there is clear evidence for extra emission on the blue wing of the Si IV λ1402.8 line. Using the same multiline fitting procedure, we measure the line fluxes given in Table 4. We note that high dispersion does not improve the flux measurements significantly, because the lines are overresolved due to rotational line broadening, and the rotational line broadening causes line blending.

TABLE 5

DENSITY DIAGNOSTICS

Lines	Ratio	$\log n_e$ (cm^{-3})	$\log n_e$[a] (cm^{-3})
Si III λ1206/Si III] λ1892	16.5 ± 0.5	12.2 ± 0.1	...
Si III λ1301/Si III] λ1892	0.42 ± 0.05	12.5 ± 0.1	...
Si III $\lambda\lambda$1294–1301/ Si III] λ1892	2.0 ± 0.2	12.2 ± 0.1	...
Si III $\lambda\lambda$1294–1301/ Si III λ1206	0.12 ± 0.01	$12.2\ ^{+0.4}_{-0.8}$	...
C III λ1247/C III] λ1908	0.25 ± 0.14	$11.1\ ^{+0.4}_{-0.2}$	...
C III λ1175/C III λ1247	157 ± 89	$9.1\ ^{+1.1}_{-0.8}$	$11.8\ ^{+2.8}_{-0.8}$
C III λ1175/C III] λ1908	39 ± 1	10.8 ± 0.1	11.1 ± 0.1
Si IV λ1402/C III] λ1908	10.6 ± 0.5	11.5 ± 0.1	...
Si III] λ1892/CIII] λ1908	1.3 ± 0.1	10.5 ± 0.1	...

[a] Density computed after doubling the C III λ1175 flux (see § 7.2).

We measure the $\lambda 1399.8/\lambda 1407.4$ line ratio to be 2.1 ± 0.5, which is marginally consistent with the expected value of 0.993. Because of the poor accuracy of the flux determinations, the density diagnostics are inconclusive. Similarly, the S IV line ratios are inconclusive. The S IV $\lambda 1423.9$ line is blended at low resolution with a stronger S I line. Although there is a weak line near 1416.9 Å in the low-dispersion spectrum, no line of similar strength is seen in the higher resolution spectrum.

7.4. *Densities of AB Dor*

The densities listed in Table 5 range from about 10^9 cm^{-3} to 3×10^{12} cm^{-3}. The densities derived from the four line ratios using the Si III lines are self-consistent but larger than the other diagnostics, while those involving C III] $\lambda 1908$ are systematically low. As discussed above, an arbitrary doubling of the C III $\lambda 1175$ line flux (justified because it appears to work for the Sun) brings the $\lambda 1175/\lambda 1247$ density into better agreement with the Si III densities (Table 5), while leaving all the densities based on C III] $\lambda 1908$ consistently lower by about an order of magnitude.

The systematically lower densities indicated by the ratios involving the C III] $\lambda 1908$ line can be reconciled if the C III] $\lambda 1908$ line is preferentially formed in the extended, low-density region near the corotation radius. This would explain both the significant broadening of the C III] $\lambda 1908$ line and the enhanced line strength. The FWHM of the C III] $\lambda 1908$ line (Table 3) corresponds to about $3v \sin i$ and so is consistent with formation in a region close to the corotation radius. We believe that the most reliable density estimate is $n_e = 2$–3×10^{12} cm^{-3} from the Si III line ratios because of the consistency among the four ratios. The electron pressure at 30,000 K would then be $P_e = n_e T = 6$–9×10^{16} cm^{-3} K, about 100 times the value for the quiet Sun.

8. EMISSION-MEASURE DISTRIBUTION

We present an emission-measure distribution based on the observed line fluxes in Figure 9. We use the line emissivities tabulated by Landini & Monsignori Fossi (1990), interpolated with a cubic spline. Landini & Monsignori Fossi computed the line emissivities in the low-density limit. Since much of the flux seems to arise in a high-density atmosphere, we used the CHIANTI database to determine the relative emissivities at low and high densities and used this to determine proper emissivities for the few density-sensitive lines. The emission-measure curves in Figure 9 assume that $n_e = 10^{12}$ cm^{-3}.

In this diagram, we have overplotted the $T^{3/2}$ extrapolation of the coronal emission measure for $\int n_e n_{\mathrm{H}} dV = 3 \times 10^{52}$ cm^{-3} at log $T = 6.6$ (Rucinski et al. 1995b; Mewe et al. 1996). We have also added the far-UV line fluxes from *Orbiting and Retrievable Far and Extreme Ultraviolet Spectrometer II* (*ORFEUS II*; Schmitt et al. 1998), after multiplying the *ORFEUS II* fluxes by 1.1 to bring their C III $\lambda 1175$ and Si III $\lambda 1206$ fluxes into agreement with our measurements. The extrapolation of the emission measure of the cooler coronal component is in good agreement with the fluxes of the C III, C IV, N V, and O VI lines, especially considering the nonsimultaneity of the UV, FUV, and X-ray observations.

A number of lines seem to have emission measures above the minimum. The cool C, Si, and S lines may either form at temperatures below log $(T) = 4.2$, or they may derive much

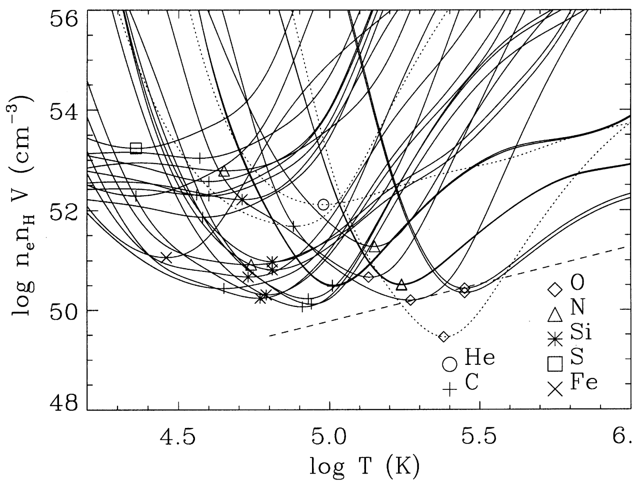

FIG. 9.—Emission-measure diagram for AB Dor. Emissivities are from Landini & Monsignori Fossi (1990), for an assumed electron density of 10^{12} cm^{-3}. The emissivity curves have been interpolated with a cubic spline. FUV data from Schmitt et al. (1997) are included, as is the $T^{3/2}$ extrapolation of the coronal emission measure from Rucinski et al. (1995b). Symbols identifying the elements are plotted at the minimum emission measures for each curve. The O V $\lambda 1371$, He II $\lambda 1640$, and C III] $\lambda 1908$ emission measures, which are explicitly discussed in § 8 of the text, are shown as dotted lines.

of their flux from a large extended volume. Three other lines are clearly out of place:

C III] $\lambda 1908$.—The implied emission measure is 1.5 orders of magnitude larger than that of the other C III lines, which is consistent with the trends from other species. No more than a few percent of the C III] $\lambda 1908$ flux can be generated at these high densities because of strong collisional deexcitation; the remainder of the flux may arise in an extended lower density region.

He II $\lambda 1640$.—The line is far too strong to be formed in collisional equilibrium at a temperature near 10^5 K (Jordan 1975), given the emission measure at this temperature. This line is more likely formed during recombination, following ionization of He I by coronal X-rays shining down on the lower chromosphere at $T \sim 10^4$ K (Zirin 1975; Laming & Feldman 1993; Wahlstrøm & Carlsson 1994).

O V $\lambda 1371$.—The flux line suggests a very small emission measure. The line emissivity in Landini & Monsignori Fossi (1990) suggests that the line should be an order of magnitude *brighter* than is observed. The O V emission measure is inconsistent with the O IV and O VI line-emission measures.

Note that the strong transition-region resonance lines of Si IV, C IV, and N V suggest emission measures somewhat above the minimum values indicated by other ions. We suggest that the excess flux, that above the minimum in the emission-measure diagram, may arise in the spatially extended gas near the corotation radius.

9. INTERSTELLAR ABSORPTION FEATURES

There is considerable evidence that the Sun lies inside a small cloud, called the Local Interstellar Cloud (LIC), of warm, partially ionized gas moving with a single-valued bulk flow velocity of -26 km s^{-1} from Galactic coordinates $l^{\mathrm{II}} = 186°$ and $b^{\mathrm{II}} = -16°$, roughly the direction of the Sco-Cen association (Crutcher 1982; Lallement et al. 1995; Redfield & Linsky 2000). In spectra of nearby stars, narrow interstellar absorption features with velocities equal to the projected velocity of the LIC vector are identified as absorption from this cloud along the line of sight to the star. Other nearby clouds that have been identified include the G Cloud, so named because it lies in the direction of the Galactic center (Lallement & Bertin 1992), and clouds in the direction of the north and south Galactic poles (Redfield & Linsky 2000). Observations of α Cen and 36 Oph indicate that the interface between the LIC and the G Cloud is located less than 0.19 pc from the Sun, roughly in the direction of the Galactic center (Linsky & Wood 1996; Wood, Linsky, & Zank 2000). A three-dimensional model of the LIC was developed by Redfield & Linsky (2000) based on 32 lines of sight using *HST*, *EUVE*, and ground-based Ca II spectra. In their model, the LIC extends about 5 pc in the anti–Galactic center direction, and a fraction of a parsec in the Galactic center direction, so that the Sun is located just inside the very edge of the LIC. The model predicts the presence of very little LIC material for the line of sight toward AB Dor.

The Mg II lines of AB Dor contain two broad interstellar absorption features. We fit the ISM features in the mean Mg II h and k lines simultaneously to maximally constrain the heliocentric velocity v (km s^{-1}), the Doppler parameter b (km s^{-1}), and the Mg II column density $\log N_{\rm Mg\,II}$ (log cm^{-2}). The best fit is illustrated in Figure 10. To estimate the "continuum" against which the absorption features are measured, we use observed fluxes on either side of the absorption features and fluxes derived from mirroring the red side of the line together to fit a fifth-degree polynomial. This continuum is shown in Figure 10 as the thin solid line. For a given set of interstellar parameters (v, b, and $N_{\rm Mg\,II}$), the profiles for the interstellar absorption features were computed and then convolved with the echelle-B LSA instrumental profile (Gilliland & Hulbert 1993). In Figure 10, the absorption profiles of the individual ISM components are shown as dotted lines, and the convolution of these components with the instrumental profile is shown as the heavy solid line. A scattered light correction was made by simply subtracting a small flux level across the whole spectrum. Numerous fits were made with different estimates of the scattered-light correction factors estimate the systematic errors. For the most part, the uncertainties are dominated by the random error. The derived parameters for these interstellar absorption components are listed in Table 6.

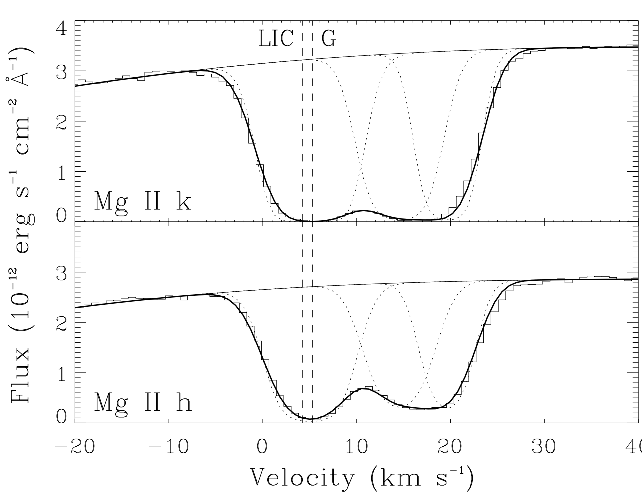

FIG. 10.—ISM absorption features observed in the Mg II lines. The velocity scale is heliocentric. The data are shown in histogram form. Our best fit to the ISM lines is also shown (see Table 6 for the fit parameters). Fifth-degree polynomial fits to a mirrored line profile (*thin solid lines*) have been used to interpolate the intrinsic Mg II line profiles in the spectral regions where the ISM absorption is located. The absorption profiles of the three interstellar absorption components are shown as dotted lines, and the convolution of the profiles with the instrumental profile is shown as a heavy solid line. Dashed vertical lines show the projected velocities of the LIC and G Cloud flow vectors for the AB Dor line of sight.

The two broad interstellar absorption features in the Mg II lines can be resolved into three different components—one with a heliocentric velocity of 5.17 km s^{-1} and the other two with velocities of 14.5 and 19.6 km s^{-1}. A two-component model inaccurately fits the high-velocity feature in the Mg II k line, so a third component was added to adequately fit the flattened appearance of the high-velocity absorption feature between 14 and 19 km s^{-1}. Since the quality of fit does not improve significantly with the addition of a fourth component, the data do not require more than three components. With a Galactic longitude of $l = 275°$ and a latitude of $b = -33°$, the projected LIC velocity toward AB Dor should be 4.25 km s^{-1}, and the corresponding G Cloud's velocity should be 5.29 km s^{-1}. Because the projected velocities of the LIC and G Cloud are so similar in value, it is difficult to interpret the observed 5.17 km s $^{-1}$ component as being associated with only one or the other cloud. The fit itself seems to favor the G Cloud projected velocity vector, and based on the LIC model and observations of other nearby stars (α Cen and 36 Oph), we expect very little LIC material along this line of sight. The LIC model predicts a hydrogen column density of $\log N_{\rm H\,I} = 16.88$ (Redfield & Linsky 2000). Using a typical magnesium depletion for the LIC of D(Mg) $\sim -1.1 \pm 0.2$ from Piskunov et al. (1997), the predicted Mg II column density contribution of the LIC in the direction of AB Dor is only $\log N_{\rm Mg\,II} \sim 11.4 \pm 0.2$, where $D({\rm Mg}) = \log (N_{\rm Mg\,II}/N_{\rm H\,I}) - \log ({\rm Mg/H})_{\odot}$. Therefore, the LIC should be a small contributor to the observed 5.17 km s^{-1} interstellar absorption component. However, if this absorption component is associated with the G Cloud, the large Doppler parameter, $b = 3.8$ km s^{-1}, implies a large turbulent velocity. If we assume a temperature typical for the G Cloud, $T = 5650$ K, based on observations of α Cen and 36 Oph (Linsky & Wood 1996; Wood et al. 2000), the turbulent velocity is then $\xi = 3.3$ km s^{-1}, where we have used the equation $b^2 = (0.0165T/A + \xi^2)$ with $A = 24.3$ for magnesium. Other turbulent velocities measured for the G Cloud by Linsky & Wood (1996) and Wood et al. (2000) have significantly lower magnitudes. This high turbulent velocity could be caused by a shearing of the gas, possibly near the interface of the cloud. However, it is more likely that because the LIC and G Cloud projected velocities are

TABLE 6

FIT PARAMETERS FOR THE Mg II INTERSTELLAR COMPONENTS

Component	v (km s^{-1})	b (km s^{-1})	$\log N_{\rm Mg\,II}$ (log cm^{-2})
1	5.2 ± 0.1	3.8 ± 0.1	13.13 ± 0.06
2	14.5 ± 0.8	3.0 ± 0.8	12.8 ± 0.4
3	19.6 ± 0.7	2.8 ± 0.5	12.7 ± 0.2

so close, we are unable to differentiate between them in the spectrum. Both clouds may be contributing to the broad absorption feature, leading to the appearance of a large Doppler parameter and turbulent velocity if the absorption is ascribed to only one cloud. The observed 14.5 and 19.6 km s^{-1} components have not yet been identified with any previously detected cloud.

10. SUMMARY

We have presented the overall quiescent characteristics of AB Doradus as it appeared during our 1994 November *HST*/GHRS observations. The transition region and Mg II line profiles provide evidence for significant amounts of material corotating with the star out to at least 3 stellar radii, with temperatures extending from the lower chromosphere to at least 10^5 K. This picture supports a model with extended gas confined near the Keplerian corotation radius (2.8 stellar radii) by large-scale magnetic fields. We surmise that most of the detected emission, the $\sim$60%–80% emitted in the narrow line component, arises in high-density, small scale height regions close to the photosphere. The extended material may well be at a lower density, as indicated by the low density derived from the Si III] λ1892/C III] λ1908 line ratio, since both lines are depleted at high density (with the C III] line depleting faster). Formation of the C III] λ 1908 line in the low-density extended gas would explain both the broad line profile and the large flux.

These quiescent spectra alone contain a wealth of information and show that high signal-to-noise ratio, high-dispersion spectra of magnetically active stellar chromospheres and coronae provide important insights into the spatial morphology of the stellar magnetospheres. In particular, we can determine the emission-measure distribution, the atmospheric densities, the spatial extent of the atmosphere, and the properties of the ISM along the line of sight. High signal-to-noise ratio, high-dispersion UV spectra of active stars provide our best indication of the conditions from which our present day solar atmosphere evolved.

This paper is based on observations made with the NASA/ESA *Hubble Space Telescope*, obtained at the Space Telescope Science Institute, which is operated by the Association of Universities for Research in Astronomy, Inc., under NASA contract NAS5-26555. This research was supported primarily by NASA grant NAG5-1862 to SUNY at Stony Brook. We also acknowledge support to the University of Colorado through grant S-56460-D. We thank the many people who contributed to the success of the *HST* and GHRS programs.

REFERENCES

Ake, T. B., Dupree, A. K., Young, P. R., Linsky, J. L., Malina, R. F., Griffiths, N. W., Siegmund, O. H. W., & Woodgate, B. E. 2000, ApJ, 538, L87
Anders, G. J., Coates, D. W., & Thompson, K. 1992, Proc. Astron. Soc. Australia, 10, 33
Ayres, T. R., Simon, T., Stern, R. A., Drake, S. A., & Brown, A. 1998, ApJ, 496, 428
Blackwell, J., Shore, S. N., Robinson, R. D., Feggans, K., Lindler, D. J., Malumuth, E., Sandoval, J., & Ake, T. B. 1993, A User's Guide to the GHRS Software (Version 2.1; Greenbelt MD: GSFC)
Brandt, J. C., et al. 1994, PASP, 106, 890
Burton, W. M., & Ridgeley, A. 1970, Sol. Phys., 14, 3
Collier Cameron, A., Duncan, D. K., Ehrenfreund, P., Foing, B. H., Kuntz, K. D., Penston, M. V., Robinson, R. D., & Soderblom, D. R. 1990, MNRAS, 247, 415
Collier Cameron, A., & Robinson, R. D. 1989, MNRAS, 238, 657
Collier Cameron, A., et al. 1999, MNRAS, 308, 493
Collier Cameron, A., & Foing, B. 1997, Observatory, 117, 218
Cook, J. W., Keenan, F. P., Dufton, P. L., Kingston, A. E., Pradhan, A. K., Zhang, H. L., Doyle, J. G., & Hayes, M. A. 1995, ApJ, 444, 936
Cook, J. W., & Nicolas, K. R. 1979, ApJ, 229, 1163
Crutcher, R. M. 1982, ApJ, 254, 82
Dere, K. P., Landi, E., Mason, H. E., Monsignori Fossi, B. C., & Young, P. R. 1997, A&AS, 125, 149
Dere, K. P., & Mason, H. E. 1993, Sol. Phys., 144, 217
Doschek, G. A., Feldman, U., Mariska, J. T., & Linsky, J. L. 1978, ApJ, 226, L35
Dufton, P. L., Hibbert, A., Kingston, A. E., & Doschek, G. A. 1982, ApJ, 257, 338
Feldman, U., Behring, W. E., Curdt, W., Schüle, U., Wilhelm, K., Lemaire, P., & Moran, T. 1997, ApJS, 113, 195
Gilliland, R. L., & Hulbert, S. J. 1993, GHRS Instrument Science Report 55 (Baltimore: STScI)
Gray, D. F. 1992, The Observation and Analysis of Stellar Photospheres (2d ed.; Cambridge: Cambridge Univ. Press)
Guirado, J. C., et al. 1997, ApJ, 490, 835
Heap, S. R., et al. 1995, PASP, 107, 871
Innis, J. L., Coates, D. W., Thompson, K., & Robinson, R. D. 1985, Proc. Astron. Soc. Australia, 6, 156
Innis, J. L., Thompson, K., & Coates, D. W. 1986, MNRAS, 223, 183
Jordan, C. 1975, MNRAS, 170, 429
Kürster, M., Schmitt, J. H. M. M., Cutispoto, G., & Dennerl, K. 1997, A&A, 320, 831
Lallement, R., & Bertin, P. 1992, A&A, 266, 479
Lallement, R., Ferlet, R., Lagrange, A. M., Lemoine, M., & Vidal–Madjar, A. 1995, A&A, 304, 461
Laming, J. M., & Feldman, U. 1993, ApJ, 403, 434
Landini, M., & Monsignori Fossi, B. C. 1990, A&AS, 82, 229
Linsky, J. L., & Wood, B. E. 1996, ApJ, 463, 254
Mewe, R., Kaastra, J. S., White, S. M., & Pallavicini, R. 1996, A&A, 315, 170
Pakull, M. W. 1981, A&A, 104, 33
Piskunov, N., Wood, B. E., Linsky, J. L., Dempsey, R. C., & Ayres, T. R. 1997, ApJ, 474, 315
Redfield, S., & Linsky, J. L. 2000, ApJ, 534, 825
Robinson, R. D., & Collier Cameron, A. 1986, Proc. Astron. Soc. Australia, 6, 308
Robinson, R. D., et al. 1998, PASP, 110, 68
Rucinski, S., Garrison, R. F., & Duffee, B. 1995a, Inf. Bull. Variable Stars, 4156, 1
Rucinski, S. M., Mewe, R., Kaastra, J. S., Vilhu, O., & White, S. M. 1995b, ApJ, 449, 900
Schmitt, J. H. M. M., Cutispoto, G., & Krautter, J. 1998, ApJ, 500, L25
Vilhu, O., Ambruster, C., Neff, J. E., Linsky, J. L., Brandenberg, A., Ilyin, L. V., & Shakovskaya, N. I. 1989, A&A, 222, 179
Vilhu, O., Gustafsson, B., & Walter, F. M. 1991, A&A, 241, 167
Vilhu, O., Muhli, P., Huovelin, J., Hakala, P., Rucinski, S. M., & Collier Cameron, A. 1998, AJ, 115, 1610
Wahlstrøm, C., & Carlsson, M. 1994, ApJ, 433, 417
Walter, F. M. 1999, in ASP Conf. Ser. 158, Solar and Stellar Activity: Similarities and Differences, ed. C. J. Butler & J. G. Doyle (San Francisco: ASP), 87
Walter, F. M., & Byrne, P. B. 1997, in ASP Conf. Ser. 154, Cool Stars, Stellar Systems, and the Sun, ed. R. Donahue & J. Bookbinder (San Francisco: ASP), 1458
Walter, F. M., et al. 1995, BAAS, 187, 103.05
Walter, F. M., Norman, D., & Kim, J. S. 2001, in preparation
Wood, B. E., Linsky, J. L., & Ayres, T. R. 1997, ApJ, 478, 745
Wood, B. E., Linsky, J. L., & Zank, G. P. 2000, ApJ, 537, 304
Zirin, H. 1975, ApJ, 199, L63